Pt@Cu₂O/WO₃ composite photocatalyst for enhanced photocatalytic water oxidation performance

Huihua Gong[a], Yifeng Zhang[a], Yue Cao[a], Maolan Luo[a], Zhicheng Feng[b], Wenbin Yang[b,*], Kewei Liu[a], Hongmei Cao[a], Hongjian Yan[a,*]

[a] College of Chemistry, Sichuan University, Sichuan 610065, PR China
[b] State Key Laboratory of Environmental Friendly Energy Materials, Southwest University of Science and Technology, Sichuan 621010, PR China

ARTICLE INFO

ABSTRACT

In this study, Pt@Cu₂O/WO₃ composite photocatalyst was constructed via coupling Cu₂O onto the edged (200) and (020) facets of square-like WO₃ nanoplates and followed by photodeposition of Pt onto Cu₂O. The remarkably enhanced photocatalytic water oxidation activity over such assembled Pt@Cu₂O/WO₃ composite photocatalyst was observed. The superior photocatalytic performance can be attributed to intrinsic nature of charge separation between different facets of square-like WO₃, highly efficient WO₃-to-Cu₂O electron transfer occurring at the intimate contact interface between WO₃ and Cu₂O, and Pt as reduction cocatalyst. This work will provide new deep insights into the design of crystal-based Z-scheme heterostructure photocatalysts by facet-preferentially coupling one semiconductor with another.

1. Introduction

Photocatalytic water oxidation for O₂ evolution is much more important and challenging in photocatalytic water splitting, because it is a multiple interactions and the removal of four-electron and four-proton for O₂ evolution [1]. Therefore, much work has been focused on the improvement of solar-to-oxygen conversion efficiency for high-efficiency water splitting [2,3]. Tungsten trioxide (WO₃), an n-type semiconductor with a band gap of 2.4–2.8 eV [4], is one of the most studied visible light-driven photocatalyst for O₂ evolution, due to its advantages of nontoxicity, stability against photocorrosion, photosensitivity, and stable physicochemical properties [5,6], Whereas, pure WO₃ still shows low photocatalytic efficiency due to quick electron–hole pair recombination and slow rate of charge transfer [5,6]. To address these limitations, many efforts have been developed, including morphology control or crystal facets tuning [7,8], deposition of co-catalysts [7], doping [4], and coupling with other semiconductors [9–13]. Among them, the coupling WO₃ with other narrow band-gap semiconductors with well-matched band structures to form WO₃-based heterojunctions, such as Cu₂O-WO₃ [5,10–13], C₃N₄-WO₃ [9,10], Ag₃PO₄-WO₃ [14], has been proven to be an effective strategy for promoting its photocatalytic performance. However, it is rarely reported that coupling of one semiconductor on the specific facets of another semiconductor with regular polyhedral morphology for constructing composite photocatalyst. Therefore, it is still a challenging task to exploit novel visible-

light-driven WO₃ based heterojuncted photocatalysts for enhancing the visible light absorption ability and photocatalytic performance.

In the past few years, WO₃ with the square-like morphology have been intensively explored as potential building blocks for photocatalysis [15,16]. Recently, it has been reported that photogenerated electrons and holes exhibit spatial separation between different facets of square-like WO₃ with predominant (002) facets exposure [17]. Moreover, the photocatalytic performance can be further improved with strategy of the selective deposition of dual-cocatalysts on different facets [18]. In order to construct a high efficiency WO₃-based photocatalyst for visible light water splitting, construction of square-like WO₃ based composites was an effective way. Cu₂O is a p-type semiconductor with a narrow band gap of 1.9–2.2 eV and a conduction band site at −1.4 ∼ −0.3 eV vs. NHE [19], and exhibits high photocatalytic properties. Many researchers have constructed Cu₂O-WO₃ heterojunction achieving a Z-scheme for the efficiency of electron-hole separation and high photocatalytic performance, because Cu₂O has suitable band edges that well match WO₃ [5,11–13]. Furthermore, the visible light absorption of Cu₂O greatly extends the absorption range of Cu₂O-WO₃ composites [20].

In this study, square-like WO₃ nanoplates with predominant (002) facets exposure were synthesized by hydrothermal method, and Cu₂O were coupled to the edged (200) and (020) facets of square-like WO₃ to assemble Cu₂O/WO₃ composite photocatalysts, which was further decorated by Pt on the surfaces of Cu₂O to fabricate Pt@Cu₂O/WO₃

composites for photocatalytic O_2 production. The as-fabricated Pt@Cu_2O/WO_3 composite photocatalyst exhibited high photocatalytic activity, attributed to the efficient charge separation derived from p–n junctions and synergistic effect of Pt co-catalysts.

2. Experimental section

2.1. Preparation of photocatalysts

2.1.1. Fabrication of square-like WO_3 nanoplates

All chemical reagents were of analytical grade and were used without further purification. The square-like WO_3 nanoplates were prepared by the facile hydrothermal synthesis process. In brief, 1.0 g of Na_2WO_4·$2H_2O$ was initially dissolved in 20 mL deionized water and magnetically stirred for 30 min at room temperature. And then 5 mL hydrochloric acid solution (18 wt%) was dropwise added into the solution during the stirring. The obtained yellow precipitate was collected by centrifugation and washed thoroughly with distilled water to eliminate Cl^-, and then transferred into a 30 mL of Teflon-lined stainless steel autoclave for hydrothermal treatment at 180 °C for 24 h. After cooled to room temperature naturally, the precipitate was harvested by centrifugation, washed with distilled water, and dried at 60 °C for overnight.

2.1.2. Synthesis of Pt/WO_3 powders (0.5 wt% Pt) by photoreduction method

0.500 g of WO_3 powder was suspended in 200 mL aqueous methanol (10% in volume) containing appropriate amount of H_2PtCl_6·$6H_2O$. The resulting suspension was then stirred and irradiated with a Xe lamp for half an hour after removing the dissolved oxygen completely. The product was collected, washed with deionized water and ethanol for several times. After drying at 60 °C for overnight, Pt/WO_3 was obtained.

2.1.3. Synthesis of Cu_2O/WO_3(A), and Pt@Cu_2O/WO_3

Ascorbic acid liquid phase reduction: In a typical synthesis of Cu_2O/WO_3(A), 10.0 mL of deionized water and 10.0 mL of ethylene glycol were mixed to form a solution in a beaker, into which 0.500 g of WO_3 powder and appropriate amount of $CuSO_4$ were added, and the suspension was vigorously stirred for more than 5 h. Subsequently, 5.0 mL freshly prepared solution of L-ascorbic acid (0.57 mol/L) was added dropwise into the above suspension, and magnetically stirred for another 2 h at room temperature. The product was centrifuged and thoroughly washed with deionized water and ethanol for several times, dried in air at 60 °C for 24 h. The obtained sample was denoted as Cu_2O/WO_3(A). Based on the as-prepared Cu_2O/WO_3(A), Pt@Cu_2O/WO_3 was prepared by the similar method as Pt/WO_3 mentioned above. Moreover, for comparison, a WO_3 sample, which was denoted as Vc-treated WO_3, was prepared by the same process as preparation of Cu_2O/WO_3(A), but without adding $CuSO_4$.

2.1.4. Synthesis of Cu_2O/WO_3(B), and Pt-Cu_2O/WO_3

Sodium borohydride liquid phase reduction: 0.500 g of WO_3 powder and 1.0 mL $CuSO_4$ (0.50 mol/L) were added into 20 mL of deionized water, followed by stirring for overnight. Subsequently, appropriate volume of a freshly prepared solution of $NaBH_4$ (0.20 mol/L) was added dropwise into the above suspension, and magnetically stirred for another 2 h at room temperature. The as-prepared samples were collected, washed with deionized water and ethanol for several times, and dried at 60 °C for overnight. The obtained sample was denoted as Cu_2O/WO_3(B). Based on the as-prepared Cu_2O/WO_3(B), Cu_2O-Pt/WO_3 was prepared by the similar method as Pt/WO_3 mentioned above.

2.2. Photocatalytic reactions

The photocatalytic water splitting O_2 evolution reactions were performed in a top-irradiation reactor vessel connected to a glass closed gas circulation system. Typically, 0.300 g of the as-prepared photocatalyst was dispersed in 200 mL of 0.01 M aqueous $AgNO_3$ solution ($AgNO_3$ acts as the sacrificial reagent). Before irradiated by a 300 W Xe lamp without cutoff filter, the reaction mixture was evacuated to completely remove air and establish the adsorption-desorption equilibrium between the solution and photocatalyst under constant magnetic stirring. The temperature of the reaction solution was maintained at 283 K by a flow of cooling water during the reaction. The evolved gases were analyzed by an online gas chromatograph equipped with a thermal conductivity detector (SPSIC, GC-112AT, argon carrier). The gas generated was analyzed every 1 h.

2.3. Characterization

Scanning electron microscope (SEM) images of the samples was performed with JSM-5900LV Scanning Electron Microscopy (SEM, JEOL, Japan). Transmission electron microscopy images (TEM), high-resolution (HR) TEM images of the samples were obtained on transmission electron microscope (TEM; Tecnai G2 F20 S-TWIN). Scanning transmission electron microscope (STEM) and energy-dispersive X-ray (EDX) mapping images of the samples were performed with Talos f200x field emission transmission electron microscope. Powder X-ray diffraction (XRD) patterns were obtained using a X-Pert Pro diffractometer with CuKα radiation (λ = 1.5406 Å) at a scanning speed of 4° min^{-1}. The UV–vis diffuse reflectance absorption spectra (DRS) were recorded on a UV–vis spectrophotometer (UV3600, Shimadzu) by using $BaSO_4$ as a reference. The photoluminescence (PL) spectra of the samples was carried out with a photoluminescence spectrophotometer (Hitachi F-7000) and the excitation wavelength was 230 nm. X-ray photoelectron spectroscopy (XPS) spectra were measured on a V4105 instrument (Thermo Electron, USA) with a MnKα radiation source. The amount of Pt and Cu element in the as-prepared samples was determined by using inductive coupled plasma atomic emission spectrometer (ICP-AES) (ARCOS). The time-resolved fluorescence decay spectra was measured on a Fluorolog-3 spectrofluorometer (Horiba JobinYvon) with a SpectraLED (280 nm, S-280, Horiba Scientific) as the excitation source and a picosecond photon detection module (PPD-850, Horiba Scientific) as the detector (λem = 475 nm).

2.4. Photoelectrochemical measurements

Photocurrent measurements and Electrochemical impedance spectroscopy (EIS) were performed on an Autolab PGSTAT 128N electrochemical workstation in a standard three-electrode configuration including a working electrode, counter electrode and reference electrode. Na_2SO_4 (0.1 M) aqueous solution was used as the electrolyte in the process of all electrochemical measurements at 0.8 V vs Ag/AgCl. Platinum foil and Ag/AgCl electrode (in saturated KCl) were used as the counter electrode and as a reference electrode, respectively. The working electrodes were prepared as follows: 0.0050 g the as prepared sample was mixed with 375 μL distilled water, 125 μL isopropyl alcohol and 10 μL of Nafion solution (5 wt%, Dupont, United States). After ultrasonic dispersion for 30 min to form a homogeneous state slurry, 50 μL of the slurry was spread onto the FTO glass for 1 cm^2 active area. The prepared electrodes were dried at 80 °C for 1 h. The photocurrent was measured for each switch on/off event under light irradiation, and Irradiation proceeded by a 500 W Xe lamp equipped with an AM 1.5 G filter (CEAULIGHT, China). Electrochemical impedance spectroscopy (EIS) experiments were carried out under the dark with a frequency range from 0.01 Hz to 100 kHz.

2.5. Apparent quantum yield estimation

Apparent quantum efficiency (QE) for water oxidation were measured under the same experimental condition, except for the addition of a cut-off filters (λ = 420). The number of incident photons was
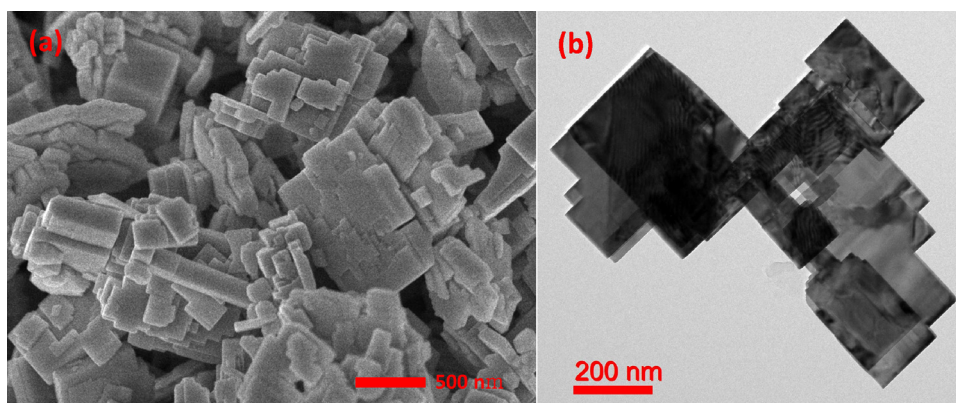
Fig. 1. SEM images (a), TEM image (b) of as-prepared square-like WO_3.

measured by using a calibrated Si photodiode. The QE was calculated according to the following equation:

$$QE\,(\%) = \frac{4 \times \text{the number of}\,O_2}{\text{the number of incident photons}} \times 100$$

3. Results and discussions

The morphology and crystalline structure of square-like WO_3 nanoplates synthesized by hydrothermal method were visualized by SEM and TEM images and shown in Fig. 1. Fig. 1a and b clearly show the square character of the WO_3 sheet with distribution from several hundred nanometres to micrometres in wide particle size and 15–20 nm in thickness. The HRTEM image (Fig. S1b, Supporting Information) reveals that the lattice fringes are 0.367 and 0.378 nm, corresponding to the (200) and (020) planes of monoclinic WO_3, respectively, which indicates that the surface of square-like WO_3 nanoplates consists of a major top (002) facets, and minor lateral (020) and (200) facets. The selected area electron diffraction (SEAD) patterns (Fig. S1c) indicated the as prepared square-like WO_3 is single crystal.

Fig. 2 displays the XRD patterns of the as-prepared WO_3, Pt/WO_3, Cu_2O/WO_3(A) and Pt@Cu_2O/WO_3, respectively. The results revealed that the prepared WO_3 was a monoclinic phase structure with obvious peaks at 2θ values of 23.15, 23.61, 24.37, 33.30, and 34.19, assigned to its (002), (020), (200), (022) and (202) facets, respectively (JCPDS No. 72-1465). And the introduction of Pt and Cu_2O did not change the crystal phase and crystallinity of WO_3. Notably, no diffraction peaks of Pt and Cu_2O except for monoclinic WO_3 were observed in the XRD patterns of Pt/WO_3, Cu_2O/WO_3(A) and Pt@Cu_2O/WO_3, which was proposed to arise from small size and high dispersion of Pt and Cu_2O, and the excessively weak response of them compared with WO_3.
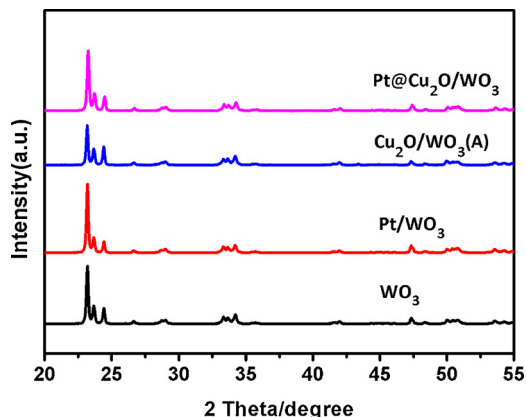
X-ray photoelectron spectroscopy (XPS) analysis presented in Fig. 3 are calibrated by referring C 1s (284.6 eV), and it has been performed to investigate surface electronic states and compositions of Cu_2O/WO_3(A). The survey spectrum (Fig. 3a) of the Cu_2O/WO_3(A) composite shows the elements W, O, Cu and C. The presence of C mainly results from the hydrocarbon from the XPS instrument itself. It is observed that $W4f_{7/2}$ and $W4f_{5/2}$ peaks are located at around 35.3 and 37.4 eV, respectively (Fig. 3b), suggesting that the W^{6+} oxidation state [18]. As shown in Fig. 3c, the O 1s region consists of three peaks located at 530.0, 531.5 and 532.9 eV. The peak at 530.0 eV could be attributed to the lattice oxygen in WO_3 [18], while the peak at 531.5 eV could be ascribed to the Cu-O in Cu_2O [21]. The other peak at 532.9 eV corresponds with surface adsorbed water [22]. Fig. 3d reveals the Cu 2p core-level spectrum. A more intense doublet peaks located at approximately 932.4 and 952.2 eV were attributed to Cu $2p_{3/2}$ and Cu $2p_{1/2}$ in Cu_2O or metal Cu [22–25], respectively. It is difficult to distinguish between Cu and Cu_2O using Cu 2p core peak because of the small difference in binding energy (0.1 eV). However, X-ray induced Cu LMM Auger peak is more sensitive to chemical state change than the Cu 2p core peak, it can distinguish Cu and Cu_2O with 568 eV and 570 eV respectively [26,27]. As shown in Fig. 3e, the peak at about 570.0 eV in the Cu LMM Auger spectra proves that the main copper species is Cu_2O. On the other hand, from Fig. 3d, a low-intensity doublet peaks with binding energies of 934.4 and 954.4 eV were assigned to Cu $2p_{3/2}$ and Cu $2p_{1/2}$ in CuO [22–25]. In addition, the shake-up satellite peaks appear at 941.6, 943.7 eV, are typically assigned to CuO due to the open $3d^9$ shell of Cu^{2+}, implying the slightly oxidation of Cu_2O surface in air under ambient conditions [28,29].

Fig. 4 displays TEM and HRTEM images of Cu_2O/WO_3(A). The TEM image (Fig. 4a) shows that the nanoparticles with diameters of 6–10 nm has been selectively coupled onto the minor edges (020) and (200) facets of square-like WO_3. These nanoparticles were uniformly dispersed on the side of WO_3. Almost very few nanoparticles were coupled to the predominant exposed (002) facets. The HRTEM image (Fig. 4b) shows the interspacing distances of 0.21 and 0.24 nm, corresponding to the interplanar distances of the (200) and (111) lattice planes of cubic-phase Cu_2O, respectively. In Fig. 4, Cu_2O/WO_3(A) was prepared through a two step route by deposition of Cu nanoparticles with L-ascorbic acid as reductant via liquid phase reduction method, and then dried and exposed in air for the oxidation of Cu nanoparticles. Copper is sensitive to air, and prone to oxidize to Cu_2O in the air [24,30–32]. Moreover, the smaller particle size, the more easily to be oxidized. Combined with previous XPS analysis results, it's believed that the nanoparticles of Cu species coupled onto the side of square-like WO_3 mainly exist as Cu_2O, trace amount of CuO only exist on the surface of Cu_2O due to the further oxidization of Cu_2O surface. The slightly oxidization of Cu_2O is beneficial because it had been found that a small amount of CuO on Cu_2O nanoparticle surface could actually serve as a protective layer to enhance its stability [25,33,34]. In short, coupling of
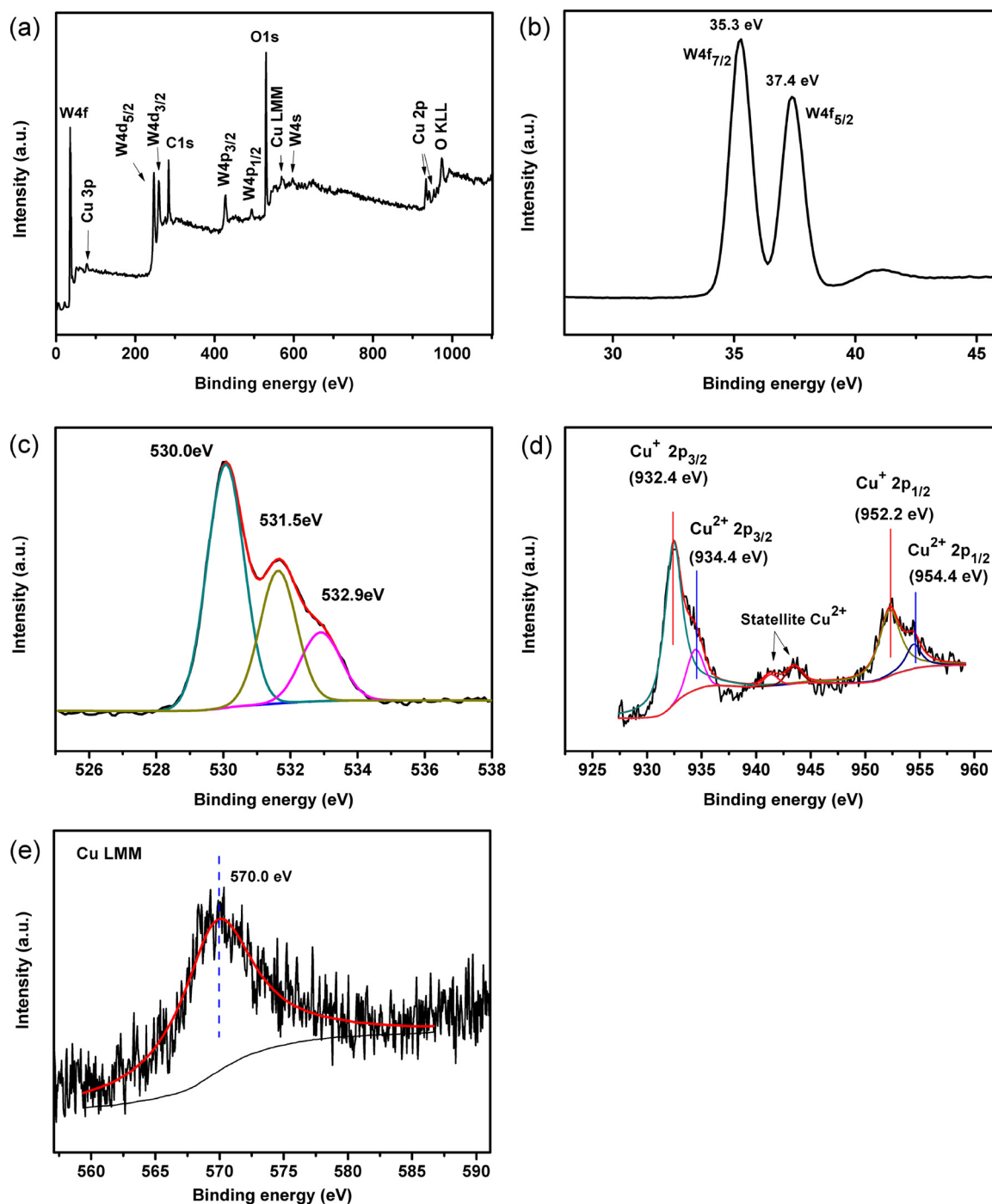

Fig. 2. XRD patterns of WO_3, Pt/WO_3, Cu_2O/WO_3(A) and Pt@Cu_2O/WO_3.

Fig. 3. XPS spectra of $Cu_2O/WO_3(A)$: wide-range (a), high-resolution spectra of W4f (b), O 1s (c), Cu2p (d), and Cu LMM Auger spectra (e).

Cu_2O nanoparticles with small particle size onto the specific facets of WO_3 has been successfully prepared.

Fig. 5 shows the TEM and HRTEM images of Pt/WO_3 (0.5 wt% Pt) prepared by the photo-reduction deposition method using $H_2[PtCl_6]$ as the precursor. It can be clearly observed that the especial locations of Pt on the square-like WO_3 surface (Fig. 5a), which is consistent with our recent work [17,18]: Pt nanoparticles with a small size of 2–3 nm were primarily loaded on the minor (200) and (020) facets of the square-like WO_3, and aggregated Pt nanoparticles were usually observed. The lattice fringes with a value of 0.227 nm (as shown in Fig. 5b) are well matched with the (111) crystal planes of metallic Pt. The phenomenon of preferred deposition of Pt may be the reason for intrinsic differences in surface charge of square-like WO_3 nanoplates leading sorption-

determined deposition of Pt on square-like WO_3 [35]. In other words, since the edges appear positively charged, the negatively charged $[PtCl_6]^{2-}$ ions adsorbed preferentially on positively charged edges prior to photoreduction, thus leading to facet-preferred photo-deposition of Pt on WO_3 [35].

Cu_2O has the same facet-preferred location as Pt (Figs. 4 and 5), which is suspected to be the similar reason for sorption-determined deposition. During the preparation of $Cu_2O/WO_3(A)$, the L-ascorbic acid solution was dropwise added. At the beginning, the concentration of L-ascorbic acid was low. Negatively charged Cu(II)-ascorbic complex ion may be formed via the reaction of Cu^{2+} with L-ascorbic acid and adsorbed on the side surfaces of WO_3 by electrostatic adsorption. With the L-ascorbic acid concentration gradually increased, Cu(II)-based complex
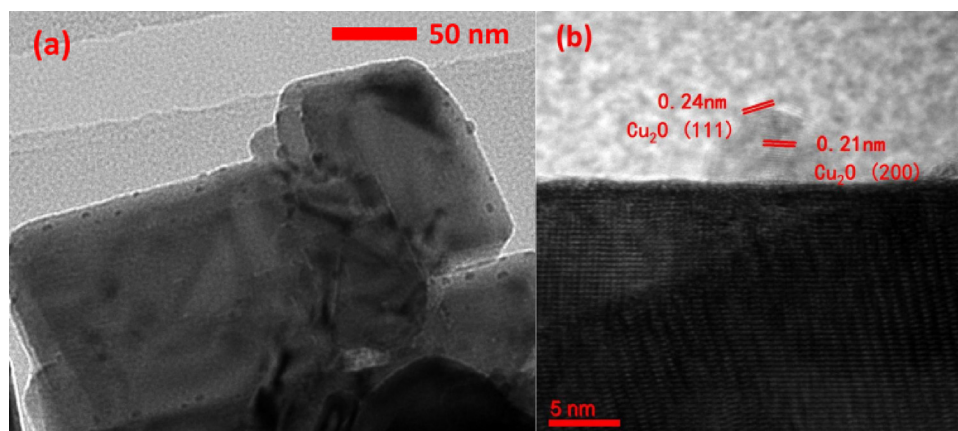
Fig. 4. TEM image (a), and HRTEM image (b) of as-prepared Cu_2O/WO_3(A). ICP-AES analysis showed that the actual Cu_2O content coupled on surfaces of WO_3 was 2.5 wt%.

ion are rapidly reduced by ascorbic acid to form Cu nanoparticles that locating on the side of WO_3 nanoplates, thus resulting the presence of Cu_2O nanoparticles on the edged (200) and (020) facets.

For comparison, another Cu_2O/WO_3 sample was prepared by using $NaBH_4$ as reductant. Fig. S3 (Supporting Information) shows the TEM and HRTEM images of Cu_2O/WO_3(B) prepared by using $NaBH_4$ as reductant. It can be observed that Cu_2O nanoparticles with a primary size of 4–8 nm were uniformly dispersed on the different crystal planes of square-like WO_3, including the edged (200) and (020) facets and the predominant (002) facets. These results indicated that by using ascorbic acid liquid-phase reduction method, Cu_2O can be selectively loaded on the edged (200) and (020) facets of square-like WO_3 (as shown in Fig. 4), while Cu_2O can be randomly distributed on the surface of the square-like WO_3 by the sodium borohydride liquid-phase reduction method (as shown in Fig. S3).

Fig. 6 shows the TEM and HRTEM images of $Pt@Cu_2O/WO_3$ prepared by photo-reduction deposition of Pt on Cu_2O/WO_3(A). After the photo-reduction deposition of Pt on Cu_2O/WO_3(A), compared to Pt/WO_3, the aggregation of Pt has been well relieved. The HRTEM images (Fig. 6b) exhibits that the interplanar spacings of 0.196, 0.227 nm corresponds to the (200) and (111) facets of Pt, and the lattice fringes of 0.21 nm assign to the (200) facets of Cu_2O. Meanwhile, it could be observed that Pt particles were deposited on the surfaces of Cu_2O nanoparticles, suggesting the intimate interfaces between Pt and Cu_2O in $Pt@Cu_2O/WO_3$. Furthermore, SEM and STEM images and the corresponding EDX spectrum of $Pt@Cu_2O/WO_3$ (shown in Figs. S5 and S6 in

Supporting information) also confirm this phenomenon. Many spherical-shaped aggregates formed by Cu_2O and Pt are mostly deposited on the edges of WO_3. This phenomenon that Pt nanoparticles were mainly loaded on the surface of Cu_2O may be due to the Z-scheme charge transfer mechanism for Cu_2O/WO_3(A). When photo-reduction deposition of Pt on Cu_2O/WO_3(A) to prepared $Pt@Cu_2O/WO_3$ composite photocatalyst, the quenching of both the CB electrons in WO_3 and the VB holes in Cu_2O would result in accumulated abundant electrons in the CB of Cu_2O and holes in the VB of WO_3 to participate in the photo-reduction($Pt^{4+} + e^- \rightarrow Pt°$) and photo-oxidation half reactions, respectively. The photoreduction reaction occurs mainly on Cu_2O, so the Pt nanoparticles were mainly deposited on the Cu_2O surfaces. The "in situ" photo-reduction deposition of Pt allows the Pt to be deposited where photogenerated electrons are the most readily available. Loaded Pt on Cu_2O surfaces forming intimate interfaces could favour the capturing photogenerated electrons and the charge separation during photocatalytic process for improving the photocatalytic efficiency.

Fig. 7 shows the influence of different Cu_2O coupling amount in $Pt@Cu_2O/WO_3$ on the rate of photocatalytic O_2 evolution from an aqueous $AgNO_3$ solution. The amount of Cu_2O decorated on surfaces of WO_3 was measured by ICP-AES analysis. As shown in Fig. 7, the photocatalytic O_2 evolution rate of $Pt@Cu_2O/WO_3$ with 0.55, 0.92, 1.5, 2.5, 2.8, 3.0 wt% loading amount of Cu_2O was 706.1, 926.1, 1058.9, 1238.6, 935.0, 772.1 $\mu mol\, g^{-1}\, h^{-1}$, respectively. The rate of photocatalytic O_2 production increased with increasing Cu_2O decorating amount up to 2.5 wt%, beyond which it began to drastically decrease.
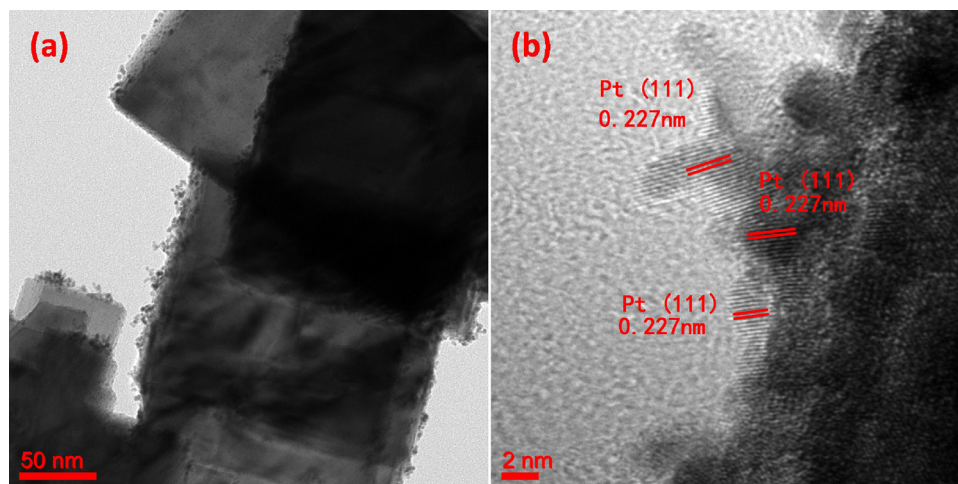

Fig. 5. TEM image (a), and HRTEM image (b) of Pt/WO_3 prepared by the photo-reduction deposition method. ICP-AES analysis showed that the actual contents of the deposited Pt was 0.46 wt%.
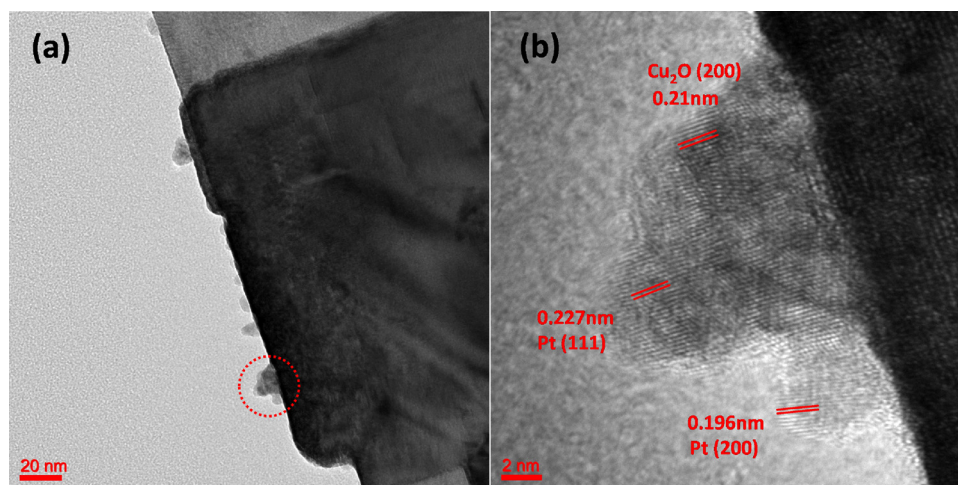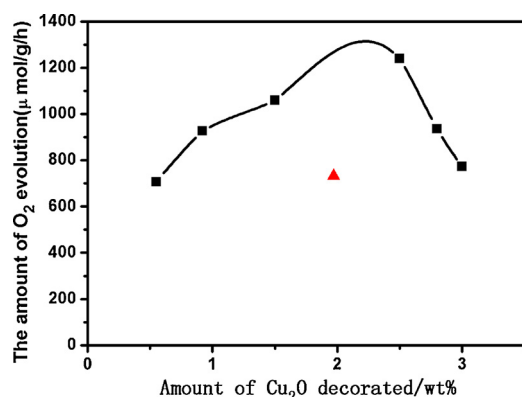
Fig. 6. TEM image (a), HRTEM image (b) of Pt@Cu$_2$O/WO$_3$.

Fig. 7. Photocatalytic water oxidation activities of Pt@Cu$_2$O/WO$_3$, which are prepared by photo-deposition of Pt on Cu$_2$O/WO$_3$(A). In all cases, the amount of Pt cocatalysts was set to be 0.5 wt%. The red triangle indicated the O$_2$ evolution rate on Cu$_2$O-Pt/WO$_3$ prepared by photo-deposition of Pt on Cu$_2$O/WO$_3$(B). Reaction conditions: 200 mL 0.01 M AgNO$_3$ aqueous solution, 300 W Xe lamp without cut-off filter, top irradiation, reaction time: 1 h. (For interpretation of the references to color in this figure legend, the reader is referred to the web version of this article).
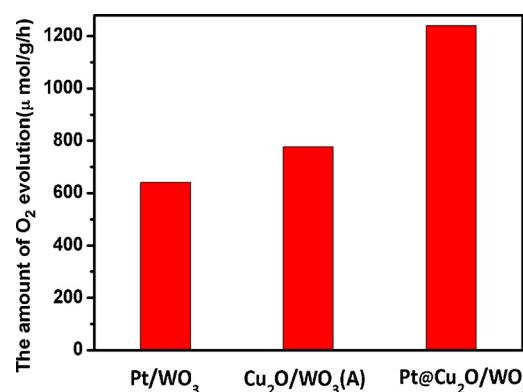

Fig. 8. Photocatalytic water oxidation activities of Pt/WO$_3$, Cu$_2$O/WO$_3$(A) and Pt@Cu$_2$O/WO$_3$. In all cases, the amount of Pt cocatalysts was set to be 0.5 wt%. Reaction conditions: 200 mL 0.01 M AgNO$_3$ aqueous solution, 300 W Xe lamp without cut-off filter, top irradiation, reaction time: 1 h.

The highest photocatalytic activity was obtained when the decorating amount of Cu$_2$O was 2.5 wt%, which was about 1238.6 $\mu mol\,g^{-1}\,h^{-1}$, corresponding to a AQE of about 1.2% at 420 nm. Besides, the red solid triangle in Fig. 7 at 1.97 wt% Cu$_2$O amount represents the photocatalytic O$_2$ evolution rate (731.9 $\mu mol\,g^{-1}\,h^{-1}$) on Cu$_2$O-Pt/WO$_3$ prepared by the deposition of Cu$_2$O on the square-like WO$_3$ with sodium borohydride as a reductant, followed by photodeposition of Pt. It shows that the photocatalytic O$_2$ evolution rate over Cu$_2$O-Pt/WO$_3$ sample was far lower than that over Pt@Cu$_2$O/WO$_3$ sample. According to the location of Cu$_2$O on Cu$_2$O-Pt/WO$_3$ sample shown in Fig. 6, we can speculate that the low rate of O$_2$ evolution over Cu$_2$O-Pt/WO$_3$ prepared by the deposition of Cu$_2$O with NaBH$_4$ as a reductant may be due to the fact that the deposition of Cu$_2$O on the predominant (002) facets of square-like WO$_3$ has no significant effect on its photocatalytic activity improvement.

Pt cocatalyst serves as an electron pool which could largely improve the catalytic activity of WO$_3$. As shown in Fig. 8, the photocatalytic O$_2$ evolution rate over Pt/WO$_3$ is 641.1 $\mu mol\,g^{-1}\,h^{-1}$, slightly lower than that over Cu$_2$O/WO$_3$(A) (777.6 $\mu mol\,g^{-1}\,h^{-1}$). Furthermore, the O$_2$ evolution rate over Pt@Cu$_2$O/WO$_3$ after loading of Pt on Cu$_2$O/WO$_3$(A) reaches 1238.6 $\mu mol\,g^{-1}\,h^{-1}$, nearly two times higher than that of Pt/WO$_3$ and 1.6 times higher than that of Cu$_2$O/WO$_3$(A). These results

indicate that coupled Cu$_2$O facet-preferentially with WO$_3$ could be a good strategy for enhanced photocatalytic performance compared to facet-preferentially deposited dual-cocatalysts for example Pt-PbO$_2$/WO$_3$ [18] system. In all cases, the theoretical amount of Pt cocatalysts was set to be 0.5 wt%. ICP-AES analysis showed that Pt loading amount of Pt/WO$_3$ and Pt@Cu$_2$O/WO$_3$ is 0.46 wt% and 0.5 wt%, which indicated that the loading rate of Pt is 93% and 100%, respectively. Namely, coupling Cu$_2$O with the edged facets of square-like WO$_3$ is beneficial to the process of photo-deposition of Pt, which indicates that constructing Z-scheme Cu$_2$O/WO$_3$(A) system facet-preferred coupling Cu$_2$O on WO$_3$ is beneficial to the efficient separation of the photo-induced electron–hole pairs and the charge carrier lifetime enhancement.

The UV–vis diffuse reflectance spectra of WO$_3$, Pt/WO$_3$, Cu$_2$O/WO$_3$(A) and Pt@Cu$_2$O/WO$_3$ were investigated and the results are shown in Fig. 9. WO$_3$ exhibited an absorption band located at 448 nm, corresponding to a band gap of 2.77 eV, and showing good absorption ability in the ultraviolet and visible regions. Pt/WO$_3$, Cu$_2$O/WO$_3$(A) and Pt@Cu$_2$O/WO$_3$ show similar absorption spectra, indicating that coupling Cu$_2$O or loading Pt on the surface of square-like WO$_3$ did not change its band gap.

Fig. 10 shows PL spectra of WO$_3$, Pt/WO$_3$, Cu$_2$O/WO$_3$(A) and Pt@Cu$_2$O/WO$_3$ under the excitation wavelength of 230 nm to investigate the separation capacity of the photogenerated carriers in heterostructures. In general, the lower PL intensity, the lower recombination rate of photoinduced electron–hole pairs, thus the higher
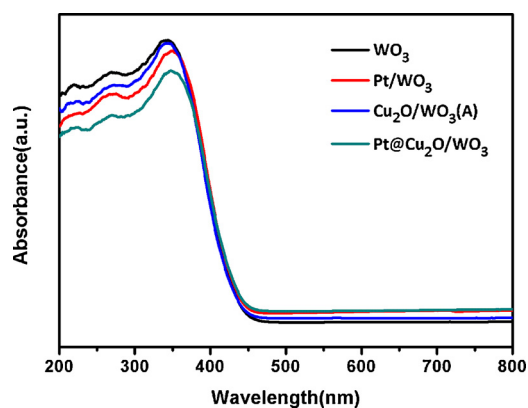
Fig. 9. UV–vis diffuse reflectance spectra of WO$_3$, Pt/WO$_3$, Cu$_2$O/WO$_3$(A) and Pt@Cu$_2$O/WO$_3$.
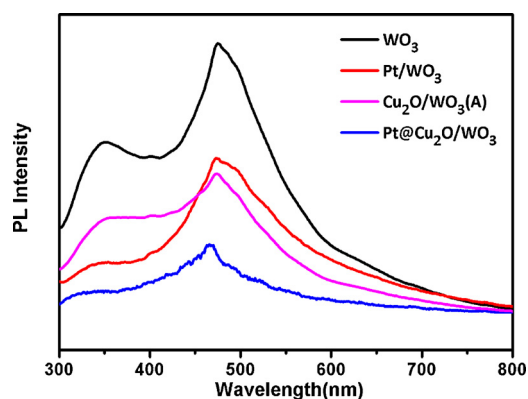
Fig. 10. Photoluminescence (PL) emission spectra of WO$_3$, Pt/WO$_3$, Cu$_2$O/WO$_3$(A) and Pt@Cu$_2$O/WO$_3$.

photocatalytic performance. As shown in Fig. 10, two emission bands in the spectra of WO$_3$ are observed. The strong blue emission band centred at 475 nm and UV emission centred at 350 nm is due to band–band indirect transition of the bulk phase WO$_3$ and the localized state of oxygen vacancies in WO$_3$, respectively [36,37]. It is clear that the peak intensities at 475 nm for Cu$_2$O/WO$_3$(A) composites is lower than that of pure WO$_3$, and the emission peak intensity of Cu$_2$O/WO$_3$(A) is slightly lower than that of Pt/WO$_3$. This result suggests that the significance p–n heterojunction formed in the Cu$_2$O/WO$_3$(A) composites is beneficial to the separation and migration of the electron–hole pairs. Notably, a drastically decreased PL intensity was observed for Pt@Cu$_2$O/WO$_3$. This indicates that the notable synergistic effect of facet-preferred deposition of Cu$_2$O on WO$_3$ as well as loading Pt co-catalysts were highly favourable for efficient separation of the photo-induced charge carriers. The change tendency of PL intensity is in good agreement with the photocatalytic performances shown in Fig. 8.

Fig. 11 presents the comparison of photocurrent–time (I–t) curves of WO$_3$, Pt/WO$_3$, Cu$_2$O/WO$_3$(A) and Pt@Cu$_2$O/WO$_3$. Significantly enhanced photocurrent were observed for Pt@Cu$_2$O/WO$_3$ and Cu$_2$O/WO$_3$ (A) compared to WO$_3$ and Pt/WO$_3$. Moreover, Pt@Cu$_2$O/WO$_3$ show a higher photocurrent density than Cu$_2$O/WO$_3$ (A), which suggests that the fast charge transfer in the Pt@Cu$_2$O/WO$_3$.

Recently, it has been reported that photogenerated charges exhibit spatial separation between different facets of square-like WO$_3$ [17,18]. In general, photogenerated holes and electrons were preferentially migrated to the dominant (002) facets and the edged (200) and (020) facets to create transient hole-rich (002) facets and electron-rich edged (200) and (020) facets, and participate in photo-oxidation and photo-reduction half reaction, respectively [17,18]. According to the band gap structures of WO$_3$ and Cu$_2$O, there are two possible separation
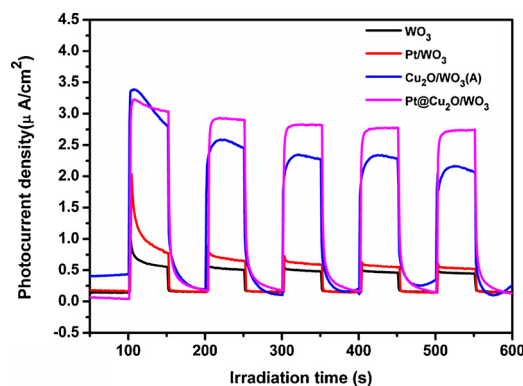

Fig. 11. Transient photocurrent responses (I–t) of WO$_3$, Pt/WO$_3$, Cu$_2$O/WO$_3$(A) and Pt@Cu$_2$O/WO$_3$ in 0.1 M Na$_2$SO$_4$ at 0.8 V vs. Ag/AgCl.

processes of photoexcited electron-holes, which can be described in Fig. 12a and b, respectively. Fig. 12a shows a traditional model for the charge transfer mechanism in composite semiconductor photocatalysts. As shown in Fig. 12a, the photogenerated electrons in the higher conduction band (CB) of Cu$_2$O will migrate to Pt and the CB of WO$_3$, and the holes in the valence band (VB) of WO$_3$ will migrate to the VB of Cu$_2$O. Due to the fact that spatial separation of photogenerated electrons and holes among the edged facets and the dominant facets of square-like WO$_3$ lead to transient hole-rich (002) facets and transient electron-rich edged facets, and the special location of Cu$_2$O on WO$_3$, if the charge carriers in Pt@Cu$_2$O/WO$_3$ composites transfer according to Fig. 12a, as a result, photogenerated electrons and holes will encounter at the interfaces between the edges of WO$_3$ and Cu$_2$O, which will promote the recombination of electrons and holes. Therefore, this model in Fig. 12a is not favorable for the enhanced photocatalytic activity of Pt@Cu$_2$O/WO$_3$. Here, the Z-scheme charge transfer mechanism (shown Fig. 12b and c) can be applied to explain the enhancement of photocatalytic O$_2$-evolution performance on the as-prepared Pt@Cu$_2$O/WO$_3$ composites. Upon simultaneous light excitation, both WO$_3$ and Cu$_2$O can be excited and generate photogenerated electron–hole pairs. Afterwards, the photogenerated e$^-$ in the conduction band (CB) of WO$_3$ can quickly transfer to edged (200) and (020) facets, where combine with the photogenerated h$^+$ in the valence band (VB) of Cu$_2$O at the interfaces of Cu$_2$O/WO$_3$ composites [15], thus preserving the holes with stronger oxidizability in the VB of WO$_3$ and the electrons with stronger reducibility in the CB of Cu$_2$O [38,39]. The photogenerated holes in the VB of WO$_3$ will oxidize water into O$_2$ and hydrogen ion, while the photogenerated electron in the CB of Cu$_2$O were captured by Pt that supported on Cu$_2$O, and then were consumed by AgNO$_3$ as the sacrificial agent to reduce Ag$^+$ to Ag. Furthermore, trace amount of CuO exist on the surface of Cu$_2$O nanoparticles that may serve as a protective layer to enhance the stability of Cu$_2$O and prevent Cu$_2$O from reacting with Ag$^+$ sacrificial reagent [25,33,34].

Namely, for square-like WO$_3$, light-induced preferential flow of photogenerated holes and electrons to the dominant (002) facets and edged (200) and (020) facets [17]. The photogenerated electrons that on the edged facets of WO$_3$ will combine with photogenerated holes of Cu$_2$O, thereby, the lifetime of holes that oriented migration on the dominant (002) facets of square-like WO$_3$ is greatly prolonged, thus enhancing O$_2$ evolution. Furthermore, photogenerated electrons of Cu$_2$O can be captured by Pt covered on the Cu$_2$O surface and quickly participate in the photoreduction half-reaction to be consumed by the sacrificial reagent. The efficient consumption of photogenerated electrons in the photoreduction reactions can simultaneously facilitate the involvement of holes in photooxidation reactions. Consequently, the Z-scheme Cu$_2$O/WO$_3$ heterostructure system and the effect of Pt cocatalysts that serve as electron sinks to trap photogenerated electron of Cu$_2$O contributed to high electron–hole separation efficiency and the
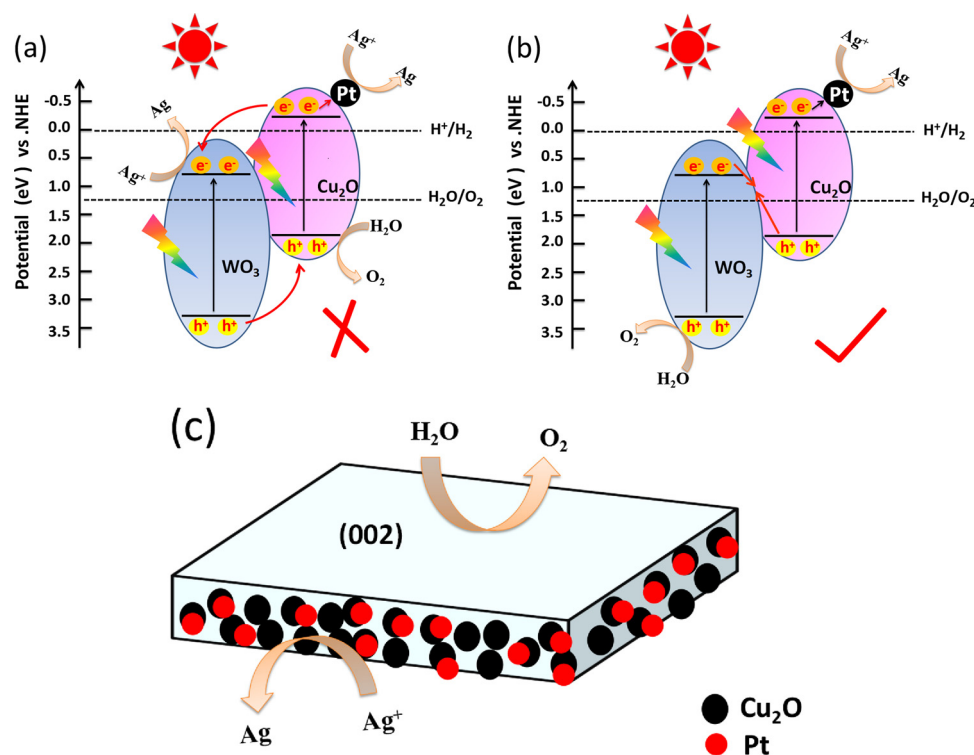
Fig. 12. Schematic diagram for photoexicited electron-hole separation processes in Pt@Cu$_2$O/WO$_3$ composite photocatalyst. (a) conventional double-charge transfer mechanism, and (b and c) direct Z-scheme mechanisms.

enhanced photocatalytic O$_2$ evolution activity on Pt@Cu$_2$O/WO$_3$ composites.

4. Conclusions

In summary, square-like WO$_3$ nanoplates were synthesized by a hydrothermal method. A direct Z-scheme Cu$_2$O/WO$_3$(A) composite photocatalytic system was successfully constructed. Cu$_2$O nanoparticles with small size of 6–10 nm has been selectively coupled onto the edged (200) and (020) facets of square-like WO$_3$. Furthermore, Pt@Cu$_2$O/WO$_3$ composite photocatalyst was achieved by loading with Pt on the surfaces of Cu$_2$O. The remarkably efficient photocatalytic ability of Pt@Cu$_2$O/WO$_3$ for photocatalytic O$_2$ production under irradiation was obtained. Spatial separation of the photogenerated charges toward different facets of square-like WO$_3$ nanoplates and facet-preferred deposition of Cu$_2$O on WO$_3$ to assemble Cu$_2$O/WO$_3$(A) system should be promising for efficient charge separation between different facets of WO$_3$ and reducing the recombination of photogenerated charge carriers in WO$_3$. Moreover, the Pt cocatalysts loading on the suitable location was also important for efficient photocatalytic water splitting over Pt@Cu$_2$O/WO$_3$. The strategy described here provides new deep insights into the design of crystal-based Z-scheme heterostructure photocatalysts by facet-preferentially coupling one semiconductor with another.

Acknowledgements

Appendix A. Supplementary data

Supplementary material related to this article can be found, in the online version, at doi:https://doi.org/10.1016/j.apcatb.2018.05.086.

References

[1] J. Yang, D. Wang, H. Han, C. Li, Acc. Chem. Res. 46 (8) (2013) 1900–1909.
[2] N. Zhang, C. Chen, Z. Mei, X. Liu, X. Qu, Y. Li, S. Li, W. Qi, Y. Zhang, J. Ye, V.A. Roy, R. Ma, ACS Appl. Mater. Interfaces 8 (2016) 10367–10374.
[3] K.A. Newton, F.E. Osterloh, Top. Catal. 59 (2016) 750–756.
[4] J.Y. Zheng, W.K. Chang, A.U. Pawar, Y.S. Kang, New J. Chem. 41 (2016) 755–762.
[5] J. Zhang, H. Ma, Z. Liu, Appl. Catal. B: Environ. 201 (2017) 84–91.
[6] J. Luo, X. Zhou, L. Ma, X. Xu, J. Mol. Catal. A: Chem. 410 (2015) 168–176.
[7] S.S.K. Ma, K. Maeda, R. Abe, K. Domen, Energy Environ. Sci. 5 (2012) 8390.
[8] D. Zhang, S. Wang, J. Zhu, H. Li, Y. Lu, Appl. Catal. B: Environ. 123–124 (2012) 398–404.
[9] H. Li, H. Yu, X. Quan, S. Chen, Y. Zhang, ACS Appl. Mater. Interfaces 8 (2016) 2111–2119.
[10] C. Cheng, J. Shi, Y. Hu, L. Guo, Nanotechnology 28 (2017) 164002.
[11] L.J. Minggu, K.H. Ng, H.A. Kadir, M.B. Kassim, Ceram. Int. 40 (2014) 16015–16021.
[12] F.E. Annanouch, Z. Haddi, S. Vallejos, P. Umek, P. Guttmann, C. Bittencourt, E. Llobet, ACS Appl. Mater. Interfaces 7 (2015) 6842–6851.
[13] T. Arai, M. Horiguchi, M. Yanagida, T. Gunji, H. Sugihara, K. Sayama, J. Phys. Chem. C 113 (2009) 6602–6609.
[14] J. Zhang, K. Yu, Y. Yu, L.-L. Lou, Z. Yang, J. Yang, S. Liu, J. Mol. Catal. A: Chem. 391 (2014) 12–18.
[15] K. Wenderich, K. Han, G. Mul, Part. Part. Syst. Charact. (2017) 1700250.
[16] Y.P. Xie, G. Liu, L. Yin, H.-M. Cheng, J. Mater. Chem. 22 (2012) 6746.
[17] H. Gong, R. Ma, F. Mao, K. Liu, H. Cao, H. Yan, Chem. Commun. 52 (2016) 11979–11982.
[18] H. Gong, Y. Cao, Y. Zhang, Y. Zhang, K. Liu, H. Cao, H. Yan, RSC Adv. 7 (2017) 19019–19025.
[19] (a) J.C. Wang, L. Zhang, W.X. Fang, J. Ren, Y.Y. Li, H.C. Yao, J.S. Wang, Z.J. Li, ACS Appl. Mater. Interfaces 7 (2015) 8631–8639.
[20] Z. Luo, H. Jiang, D. Li, L. Hu, W. Geng, P. Wei, P. Ouyang, RSC Adv. 4 (2014) 17797.
[21] W. Zhang, X. Yang, Q. Zhu, K. Wang, J. Lu, M. Chen, Z. Yang, Ind. Eng. Chem. Res. 53 (2014) 16316–16323.
[22] J.J. Teo, Y. Chang, H.C. Zeng, Langmuir 22 (2006) 7369–7377.
[23] P. Wang, Y.H. Ng, R. Amal, Nanoscale 5 (2013) 2952–2958.
[24] X.-J. Lv, S.-X. Zhou, C. Zhang, H.-X. Chang, Y. Chen, W.-F. Fu, J. Mater. Chem. 22 (2012) 18542.
[25] L. Liu, W. Yang, Q. Li, S. Gao, J.K. Shang, ACS Appl. Mater. Interfaces 6 (2014) 5629–5639.
[26] L. Pan, J.-J. Zou, T. Zhang, S. Wang, Z. Li, L. Wang, X. Zhang, J. Phys. Chem. C 118 (2013) 16335–16343.
[27] T. Ghodselahi, M.A. Vesaghi, A. Shafiekhani, A. Baghizadeh, M. Lameii, Appl. Surf.

Sci. 255 (2008) 2730–2734.

[28] J. Xiong, Z. Li, J. Chen, S. Zhang, L. Wang, S. Dou, ACS Appl. Mater. Interfaces 6 (2014) 15716–15725.

[29] X. Deng, C. Wang, E. Zhou, J. Huang, M. Shao, X. Wei, X. Liu, M. Ding, X. Xu, Nanoscale Res. Lett. 11 (2016) 29.

[30] M.D. Susman, Y. Feldman, A. Vaskevich, I. Rubinstein, Chem. Mater. 24 (2012) 2501–2508.

[31] H. Liu, T. Wang, H. Zeng, Part. Part. Syst. Charact. 32 (2015) 869–873.

[32] M. He, L. Lu, J. Zhang, D. Li, Sci. Bull. 60 (2015) 227–234.

[33] P.-Y. Kuang, X.-J. Zheng, J. Lin, X.-B. Huang, N. Li, X. Li, Z.-Q. Liu, ACS Omega 2 (2017) 852–863.

[34] P. Mao, Y. Liu, Y. Jiao, S. Chen, Y. Yang, Chemosphere 164 (2016) 396–403.

[35] K. Wenderich, A. Klaassen, I. Siretanu, F. Mugele, G. Mul, Angew. Chem. Int. Ed. 53 (2014) 12476–12479.

[36] H. Yan, X. Zhang, S. Zhou, X. Xie, Y. Luo, Y. Yu, J. Alloys Compd. 509 (2011) L232–L235.

[37] J. Meng, J. Pei, Z. He, S. Wu, Q. Lin, X. Wei, J. Li, Z. Zhang, RSC Adv. 7 (2017) 24097–24104.

[38] W. Yu, D. Xu, T. Peng, J. Mater. Chem. A 3 (2015) 19936–19947.

[39] B. Qiu, Q. Zhu, M. Du, L. Fan, M. Xing, J. Zhang, Angew. Chem. Int. Ed. 56 (2017) 2684–2688.